Trapping capability of circular swallowtail beams

Huanpeng Liang, Xiaofang Lu, Kaijian Chen[ORCID], Haixia Wu, Nana Liu, Liu Tan[ORCID], Shaozhou Jiang[ORCID], and Yi Liang[*]

Guangxi Key Lab for Relativistic Astrophysics, Center on Nanoenergy Research, Guangxi Colleges and Universities Key Laboratory of Blue Energy and Systems Integration, School of Physical Science and Technology, Guangxi University, Nanning, Guangxi 530004, China

Circular swallowtail beams (CSBs) with their remarkable autofocusing capability have garnered significant interest due to their potential applications in optical trapping. This study delves into a comprehensive investigation of the trapping force properties of CSBs. Through a combination of experimental observations and theoretical analyses, we systematically explore the quantitative manipulation of trapping forces by adjusting specific parameters. This detailed investigation provides insights into the trapping force performance and stability of CSBs. In detail, our findings reveal a consistent extension of the focal length as scale factor increases, accompanied by a reduction in the focal peak intensity, intensity contrast, and largest trapping force. Notably, the alteration in trapping force exhibits greater sensitivity compared to that of intensity and intensity contrast. Furthermore, the experimental validation of particle trapping using CSBs underscores their effectiveness, emphasizing their significant potential for optical manipulation and trapping applications.

I. INTRODUCTION

Various accelerating beams that propagate along curved trajectories have attracted a lot of attention due to the huge potential for many applications including optical tweezers [1–3], biomedical imaging [4,5], optical communication [6], and so on. The most famous accelerating beams, named Airy beams [7–12], were experimentally generated in 2007. Airy beams can be described as a result of the fold catastrophe in catastrophe theory. There are seven fundamental catastrophes including fold catastrophe [7], cusp catastrophe [13], swallowtail catastrophe [14], butterfly catastrophe [14], elliptic umbilic catastrophe [15], hyperbolic umbilic catastrophe [16], and parabolic umbilic catastrophe [17]. Most beams related to these catastrophes can present a curve propagation trajectory, and therefore, they can be employed to generate a transversely accelerating beam. For instance, a family of accelerating beams known as Pearcey beams [13,18] arises from the cusp catastrophe. Recently, another type of high-order accelerating beams called Swallowtail beams have emerged, originating from the swallowtail catastrophe [19]. Swallowtail beams display a distinctive characteristic: by tuning control parameters, they not only can evolve into higher-order butterfly catastrophes during propagation, but also can regress to lower-order cusp catastrophe, such as Pearcey beams.

As we know, autofocusing beams [20–24] are derived from radially symmetric Airy beams expressed as $\text{Ai}[(r_0 - r)/w_0]\exp[\alpha(r_0 - r)/w_0]$, where r_0 controls the radius of the Airy ring at the input (thus governing the initial position of the main lobe of the Airy function), α represents an exponential truncation factor, and w_0 influences the scale of radial

acceleration, enabling the concentration of intensity into a focal point along the propagation direction. Therefore, the autofocusing properties are intricately linked to radial acceleration and can be adjusted by manipulating parameters such as r_0, α, and w_0 [25]. Along this line, autofocusing beams based on Swallowtail beams such as circular swallowtail beams (CSBs) also show a similar autofocusing property [14,26–32]. Introduced just a few years ago, CSBs represent a cutting-edge advancement, demonstrating superior autofocusing capability compared to existing autofocusing beams like circular Airy beams. This renders them highly attractive for applications in optical manipulation. However, despite the growing interest in autofocusing beams, previous work has not comprehensively analyzed the trapping capability of CSBs, especially in experiments.

Thus, in this paper, we conduct a comprehensive investigation on trapping force and the stability of CSBs. Different from previous works [33,34], a significant portion of this study focuses on trapping and manipulating particles, underscoring the practical utility of autofocusing beams. Initially, we delve into the autofocusing characteristics of CSBs through both experimental and theoretical approaches. Subsequently, we extend our analysis to the trapping performance on Rayleigh particles, providing theoretical insights into the trapping forces exerted by CSBs. In addition, previous works [33,34] have not comprehensively analyzed the trapping capabilities of these beams for particles, especially the trapping stability. Here, we fill this gap by incorporating an analysis of trapping stability. This multifaceted exploration provides a holistic understanding of CSBs' strengths and limitations, enriching our knowledge and facilitating the development of more efficient optical manipulation techniques. To validate our findings, we employ CSBs as optical tweezers in experiment, trapping Mie particles, and measuring the trap stiffness.

---

[*]Contact author: liangyi@gxu.edu.cn

Remarkably, our results agree well with those calculated using generalized Lorentzian Mie theory, confirming the accuracy and reliability of CSBs in optical trapping applications. This work significantly contributes to the understanding of the optical trapping capability of CSBs, paving the way for the application of these innovative tools in optical manipulation and trapping scenarios.

II. PROPAGATION OF CSBs

Based on catastrophe theory, a caustic field with a standard diffraction integral is given by [14]

$$\psi_n(\mathbf{a}) = \int_{-\infty}^{+\infty} \exp[ip_n(\mathbf{a}, s)]ds, \qquad (1)$$

where $p_n(\mathbf{a}, s)$ is the canonical potential function that can determine the properties of the caustic field, and it is defined by [14]

$$p_n(\mathbf{a}, s) = s^n + \sum_{j=1}^{n-2} a_j s^j. \qquad (2)$$

Here, $\mathbf{a} = (a_1, a_2, \ldots, a_j)$ are the control parameters and s is the state variable of the diffraction integral in Eq. (1). So, a Swallowtail beam can be expressed by a swallowtail catastrophe integral [27]

$$Sw(X, Y, Z) = \int_{-\infty}^{+\infty} \exp\{[i(s^5 + Zs^3 + Ys^2 + Xs^1)]\}ds, \qquad (3)$$

where X, Y, Z denote the dimensionless coordinates in the real space.

To simply construct a circular swallowtail beam, Eq. (3) can be transformed into a expression in cylindrical coordinates [27]

$$\Phi(r, \theta, 0) = Sw\left(\frac{r_0 - r}{w_0}, 0, 0\right)Q(r, \theta). \qquad (4)$$

As previously introduced, r_0 controls the initial radius of the main ring, while w_0 serves as the scale factor influencing radial acceleration. Additionally, w_0 determines the quantity and width of the rings. The function $Q(r)$ acts as a transmittance function, confining the beams within a specified distribution range, thereby guaranteeing finite energy and feasibility for experimental realization. It is defined as follows:

$$Q(r, \theta) = \begin{cases} 1, & 0 \leqslant r \leqslant R_B, 0 \leqslant \theta \leqslant 2\pi, \\ 0, & \text{other}, \end{cases} \qquad (5)$$

where R_B is the radius of the CSBs in the initial plane.

In paraxial approximation, the propagation of Swallowtail beams follows the below wave equation [27]:

$$2i\frac{\partial \Phi}{\partial z} + \frac{\partial^2 \Phi}{\partial r^2} + r^{-1}\frac{\partial \Phi}{\partial r} + r^{-2}\frac{\partial \Phi}{\partial \theta} = 0. \qquad (6)$$

Then, similar to the previous works, we can apply beam propagation methods to simulate the propagation of CSBs and analyze their autofocusing property. In the experiment, CSBs were generated using holographic techniques, as depicted in Fig. 1(a). The hologram was loaded onto a transmissive spatial
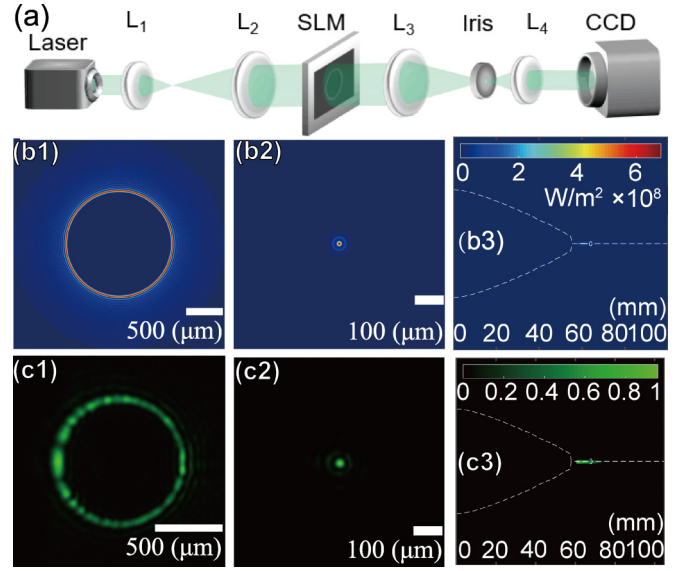

FIG. 1. Propagation of CSBs. (a) Experiment setup: Laser (532 nm), semiconductor laser. L, lens. SLM, spatial light modulator. (b1), (b2) Numerical results at $z = 0$ mm, 61 mm. (b3) Numerical propagation sideview. (c1)–(c3) corresponding experimental results.

light modulator (SLM) (1024×768, pixel pitch is 36 μm, fill factor is 58%). A linearly polarized Gaussian beam was emitted from the semiconductor laser (532 nm) and was subsequently expanded by lenses (L1 and L2). Upon passing through the SLM, the beam was transformed into a CSB with the necessary information via a $4f$ system (L3 and L4). The initial intensity distribution of the CSBs appeared at the focal plane of L4, and the propagation of CSBs was recorded by adjusting the CCD camera position. In both simulation and experiment, the parameters were set as follows: $R_B = 1.4$ mm, $r_0 = 0.7$ mm, $w_0 = 8.33$ μm.

Figures 1(b) and 1(c) display the numerical and experimental propagation results of CSBs including the intensity distributions at $z = 0$ mm, 61 mm, and their propagation sideview. Obviously, at the beginning, the main ring of CSB exhibits maximum intensity [Fig. 1(b1)]. When the beam reaches the position of $z = 61$ mm [Fig. 1(b2)], all the power converges automatically to a very small spot, with a radius of about 10.5 μm. Thus, CSB exhibits an autofocusing property without any lens in free space. Figures 1(b3) and 1(c3) present the side view of propagation, where the dashed lines represent the trajectories of the main rings, showing clear evidence of autofocusing. In Fig. 1(c), we present the experimental results, which demonstrates a close alignment with the simulated outcomes. Both results exhibit similar focal lengths and autofocusing propagation characteristics. However, it is crucial to highlight a notable distinction: while the simulation shows an amplitude distribution featuring a primary ring carrying the most energy and several thinner rings carrying less energy, only the primary ring is observed in the experimental results. This deviation can be attributed to various experimental factors, such as the low diffraction efficiency of the spatial light modulator, which poses challenges for the manifestation of the thinner rings in the experimental setup.
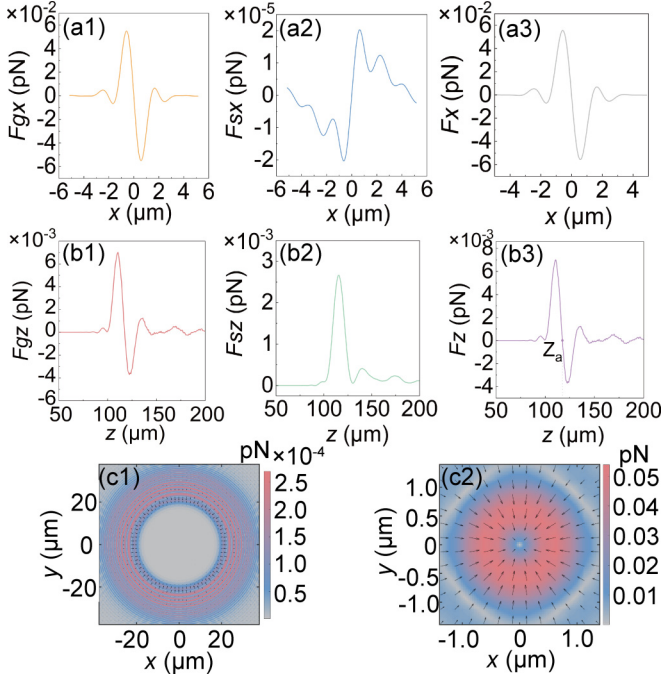
FIG. 2. Distribution of trapping force of a CSB with the parameters as follows: $R_B = 50\,\mu m$, $r_0 = 25\,\mu m$, $w_0 = 0.7\,\mu m$, the incident power for simulation is set to be 1 W, the radius of polystyrene particles is 46 nm, the focal length is $116.29\,\mu m$. Z_a denotes the longitudinal trapping position at the focus. (a1) Transversal gradient force (F_{gx}) at Z_a. (a2) Transversal scattering force (F_{sx}) at Z_a. (a3) Transversal total force (F_x) at Z_a. (b1) Longitudinal gradient force (F_{gz}). b(2) Longitudinal scattering force (F_{sz}). (b3) Total longitudinal force (F_z). (c1) Force distribution at $z = 30\,\mu m$. (c2) Force distribution at the focus.

III. TRAPPING PERFORMANCE OF CSBs ON RAYLEIGH PARTICLES

According to the theory, the gradient force $\vec{F}_g$ and the scattering force $\vec{F}_s$ of the Rayleigh particles can be calculated by [33,34]

$$\vec{F}_g = \frac{1}{4}\varepsilon_0\varepsilon_m \mathrm{Re}(\alpha)\nabla|\Phi^2|\hat{r}, \tag{7}$$

$$\vec{F}_s = \frac{1}{6\pi c}\epsilon_m^3 k_0^4 |\alpha^2|\vec{S}, \tag{8}$$

where ϵ_m is the permittivity of the medium around the particle, ϵ_0 is the vacuum permittivity, k_0 is the wave number, and $\alpha = 4\pi R_P^3(\varepsilon_p - \varepsilon_m)/(\varepsilon_p + 2\varepsilon_m)$ is the polarizability (R_P is the radius of the Rayleigh particle). $\vec{S}$ is the Poynting vector, which can be calculated by [11,35]

$$\vec{S} = \vec{S}_z + \vec{S}_\perp = \frac{1}{2\eta_0}|\Phi^2|\hat{z} + \frac{i}{4\eta_0 k}[\Phi\nabla_\perp\Phi^* - \Phi^*\nabla_\perp\Phi]. \tag{9}$$

Here, $\eta_0 = \sqrt{\mu_0/\varepsilon_0}$ is the impedance of free space, where μ_0 is vacuum permeability.

Figure 2 presents the calculated trapping force results of CSBs with a focal spot of $2.76\,\mu m$ while trapping Rayleigh polystyrene particles of $R_P = 46\,nm$ in water ($\varepsilon_m = 1.77$, $\varepsilon_p = 2.47$). As illustrated in Figs. 2(a1) and 2(a2) and

TABLE I. Trapping stability analysis.

F_b(pN)	F_{gx}(pN)	F_{gz}(pN)	ξ
2.40×10^{-3}	5.32×10^{-2}	5.26×10^{-3}	1.94×10^{-5}

Figs. 2(b1) and 2(b2), both the transversal and longitudinal gradient forces are larger than the scattering force at the focus. Furthermore, we find that the total axial trapping force exceeds the difference between buoyancy and gravity (about 2×10^{-10} pN). In this case, CSBs can trap the aforementioned particles stably. Note that all force vectors are directed toward the center of the beams [Figs. 2(c1) and 2(c2)], indicating that there is only one transverse trapping position where surrounding particles are pulled toward the center.

To further investigate the trapping stability of CSBs, we calculate the related parameters including the Brownian force F_b of the trapped particle and the Boltzmann factor ξ as follows [25,36,37]:

$$F_b = \sqrt{12\pi\eta R_p k_B T}, \tag{10}$$

$$\xi = \exp(-U/k_B T), \tag{11}$$

where $U = \frac{1}{4}\varepsilon_0\varepsilon_m\mathrm{Re}(\alpha)\Delta|\Phi^2|$ is the potential energy of the gradient force, $\Delta|\Phi^2|$ denotes the intensity difference related to the potential energy of the gradient force, k_B represents the Boltzmann constant, T is the thermodynamic temperature of medium (here we assume that the $T = 300$ K), and η denotes the viscosity of the surrounding medium (water, $\eta = 8 \times 10^{-4}$ Pa/s). The calculation results related to the trapping stability are presented in Table I. Clearly, both the transversal gradient force (F_{gx}) and longitudinal gradient force (F_{gz}) can overcome the Brownian force (F_b). Moreover, the Boltzmann factor (ξ) is much smaller than 1, indicating that the time to trap a particle is much less than the time to leave the trap due to Brownian motion [36]. Thus, it can be inferred that the above Rayleigh particles can be stably trapped by CSBs.

IV. TUNING THE AUTOFOCUSING AND TRAPPING FORCE PROPERTIES

As we know, r_0 controls the radius of the main ring at the source plane, while w_0 governs the width of the main ring and the number of rings in the source plane. Both parameters influence the focal spot size and further the autofocusing intensity. Thus, by systematically adjusting these parameters of CSBs, we can analyze the quantitative variations in autofocusing and trapping force at the focus, as depicted in Fig. 3. From Fig. 3, one can see that the distribution of focal peak intensity ($I_{\max}$) in Fig. 3(b) is different from the intensity contrast K (K is the ratio between the maximum intensity at the focus and the maximum intensity at the initial plane) [Fig. 3(a)]. It is evident that, with an increase in w_0, the focal length undergoes a consistent increase, while both the focal peak intensity ($I_{\max}$) and intensity contrast (K) decrease. Additionally, the largest trapping force also decreases as w_0 increases. For each w_0 value, there exists an optimal r_0 (approximately $500\,\mu m$) that maximizes these results. However, while w_0 varies, the change in trapping force is more pronounced compared to that

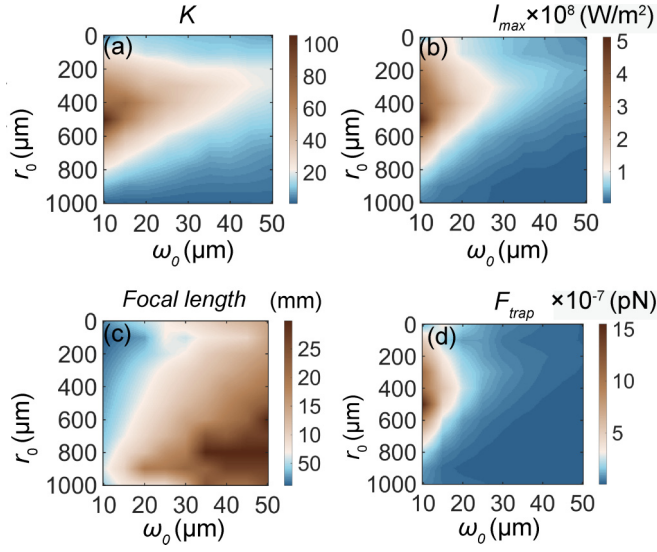FIG. 3. Autofocusing and trapping-force performance of CSBs with varying parameters r_0 and w_0. R_B is set to be 2 mm, the incident power is set to be 1 W, the wavelength is 1064 nm, the radius of polystyrene particle is 20 nm. (a) The autofocusing properties, $K = I_{\max}/I_0$, $I_{\max}$ is the focal peak intensity, I_0 is the peak intensity at initial plane. (b) The focal peak intensity $I_{\max}$. (c) The autofocusing length f_z. (d) The trapping force F_{trap}.

of intensity and intensity contrast under the same conditions, indicating that the trapping force of CSBs is more sensitive to parameter variations.

V. TRAPPING PERFORMANCE OF CSBs ON MIE PARTICLES

Finally, to investigate the trapping performance of CSBs on Mie particles, we utilize the CSBs as optical tweezers to trap large polystyrene beads of different sizes in water (see video within the Supplemental Material [38]). As shown in Fig. 4(a), we employ a similar experimental setup as in Refs. [33,35]: The CSB was generated at the focal plane of Lens 4 (source plane of the CSB), and subsequently relayed to the sample using a 4-f imaging system comprised of Lens 5 and Oil Lens. By adjusting the distance between Lens 4 and Lens 5, we place the autofocusing position right at the focal point of Oil Lens. This enables us to establish optical tweezers based on CSBs for trapping polystyrene beads. Subsequently, we employ power spectrum methods [33,35] to analyze the trap stiffness of the beams.

In detail, to measure the trap stiffness, we collect scattered light from beads using a condenser lens and a quadrant photodiode (QPD) to record the real-time positions of the trapped beads. These positions were then transformed into a power spectrum for calculating the trap stiffness. Specifically, the trap stiffness ($\kappa_r = -dF_{\text{trap}}/dr$) of the beams was calculated from the experimental data of the real-time trapped bead positions using the Langevin equation and the corner frequency power spectrum ($f_{c,r}$): $f_{c,r} = \kappa_r/2\pi\gamma$. Here, γ represents the particle friction coefficient ($\gamma = 3\pi\eta D_P$), where η is the viscosity of the solution and $D_P = 2R_P$ is the diameter of the trapped object.
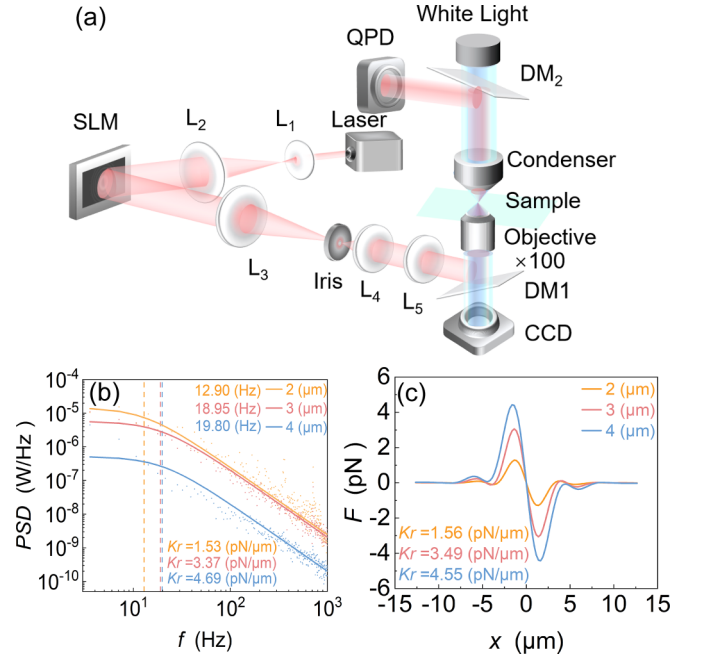

FIG. 4. (a) The experimental setup for trapping and observing particles. Laser, wavelength is 1064 nm. SLM, Spatial Light Modulator. CCD, Charged Coupled Device. Objective, oil objective lens ($\times100$), the numerical aperture is 1.25. DM, Dichroic Mirror. QPD, quadrant photoelectric detector. Beam power is set to be 20 mW. (b) Power spectra and trap stiffness of trapped polystyrene particles with a diameter of 2–4 μm. (c) Corresponding theoretical trapping force distribution and trap stiffness of these particles.

Figures 4(b) and 4(c) present the experimental results of trap stiffness when the diameter of trapped particles varies from 2 μm to 4 μm (with a light power of 20 mW). The colored dashed line and solid line [Fig. 4(b)] indicate the corner frequency. Clearly, trap stiffness increases with larger trapped Mie particles. In theory, since the size of the experimental polystyrene bead is larger than wavelength, the full-wave generalized Lorenz-Mie theory and Maxwell stress tensor technique [33,35] is used to calculate the trapping force and trap stiffness. As demonstrated in Fig. 4(c), the theoretical results are consistent with our experimental results. Trap stiffness still becomes larger when the size of the trapped Mie particles increases.

VI. CONCLUSION

In summary, our study offers a systematic exploration of the tunable autofocusing propagation and trapping performance of CSBs by manipulating beam parameters. Our findings reveal that, as the parameter w_0 increases, the focal length consistently extends, accompanied by a reduction in the focal peak intensity, intensity contrast, and largest trapping force. Notably, for each w_0 value, an optimal r_0 exists, maximizing these outcomes. Specifically, the alteration in trapping force exhibits greater sensitivity compared to that of intensity and intensity contrast. Furthermore, we assess the trapping stability of Rayleigh particles and demonstrate their stable trapping by CSBs. Finally, we utilize CSBs as optical tweezers to trap Mie particles and measure the trapping stiffness. Our

results indicate effective trapping of these particles by CSBs, with the trapping stiffness increasing proportionally with particle size, as validated by theory and experiment. Our work contributes to the field of optical trapping using autofocusing beams, offering novel photonic tools for optical tweezers and manipulation.

[1] J. Chen, C. H. Wan, and Q. W. Zhan, Adv. Photonics **3**, 064001 (2021).

[2] Y. J. Yang, Y. X. Ren, M. Z. Chen, Y. Arita, and C. Rosales-Guzman, Adv. Photonics **3**, 034001 (2021).

[3] J. Baumgartl, M. Mazilu, and K. Dholakia, Nat. Photon. **2**, 675 (2008).

[4] T. Vettenburg, H. I. C. Dalgarno, J. Nylk, C. Coll-Lladó, D. E. K. Ferrier, T. Čižmár, F. J. Gunn-Moore, and K. Dholakia, Nat. Methods **11**, 541 (2014).

[5] S. Jia, J. C. Vaughan, and X. Zhuang, Nat. Photon. **8**, 302 (2014).

[6] Y. Liang, Y. Hu, D. Song, C. Lou, X. Zhang, Z. Chen, and J. Xu, Opt. Lett. **40**, 5686 (2015).

[7] G. A. Siviloglou and D. N. Christodoulides, Opt. Lett. **32**, 979 (2007).

[8] H. Cheng, W. P. Zang, W. Y. Zhou, and J. G. Tian, Opt. Express **18**, 20384 (2010).

[9] Z. Zheng, B. F. Zhang, H. Chen, J. P. Ding, and H. T. Wang, Appl. Opt. **50**, 43 (2011).

[10] I. Kaminer, M. Segev, and D. N. Christodoulides, Phys. Rev. Lett. **106**, 213903 (2011).

[11] J. Broky, G. A. Siviloglou, A. Dogariu, and D. N. Christodoulides, Opt. Express **16**, 12880 (2008).

[12] P. Zhang, J. Prakash, Z. Zhang, M. S. Mills, N. K. Efremidis, D. N. Christodoulides, and Z. G. Chen, Opt. Lett. **36**, 2883 (2011).

[13] J. D. Ring, J. Lindberg, A. Mourka, M. Mazilu, K. Dholakia, and M. R. Dennis, Opt. Express **20**, 18955 (2012).

[14] A. Zannotti, F. Diebel, M. Boguslawski, and C. Denz, New J. Phys. **19**, 053004 (2017).

[15] Z. Sun, J. T. Hu, Y. S. Wang, W. N. Ye, Y. X. Qian, and X. Z. Li, Opt. Express **31**, 7480 (2023).

[16] N. C. Zhang, J. Q. Song, D. M. Li, X. Y. Tong, T. Li, M. L. Sun, X. X. Ma, X. Zhang, K. K. Huang, and X. H. Lu, Opt. Express **30**, 32978 (2022).

[17] Z. Sun, J. T. Hu, Y. S. Wang, W. N. Ye, and Y. X. Qian, Results Phys. **52**, 106806 (2023).

[18] X. Y. Chen, D. M. Deng, J. L. Zhuang, X. Peng, D. D. Li, L. P. Zhang, F. Zhao, X. B. Yang, H. Z. Liu, and G. H. Wang, Opt. Lett. **43**, 3626 (2018).

[19] A. Zannotti, F. Diebel, and C. Denz, Optica **4**, 1157 (2017).

[20] M. A. Bandres and J. C. Gutierrez-Vega, Opt. Express **15**, 16719 (2007).

[21] G. A. Siviloglou, J. Broky, A. Dogariu, and D. N. Christodoulides, Phys. Rev. Lett. **99**, 213901 (2007).

[22] H. I. Sztul and R. R. Alfano, Opt. Express **16**, 9411 (2008).

[23] E. Granot and B. Malomed, J. Phys. B **44**, 175005 (2011).

[24] N. K. Efremidis, Z. G. Chen, M. Segev, and D. N. Christodoulides, Optica **6**, 686 (2019).

[25] Y. F. Jiang, K. K. Huang, and X. H. Lu, Opt. Express **21**, 24413 (2013).

[26] K. Cheng, G. Lu, and X. Q. Zhong, Opt. Commun. **396**, 58 (2017).

[27] H. A. Teng, Y. X. Qian, Y. P. Lan, and Y. M. Cai, Opt. Lett. **46**, 270 (2021).

[28] H. A. Teng, Y. X. Qian, Y. P. Lan, and W. T. Cui, Opt. Express **29**, 3786 (2021).

[29] J. J. Jiang, D. L. Xu, Z. W. Mo, X. Z. Cai, H. Y. Huang, Y. Zhang, H. B. Yang, H. Q. Huang, Y. Wu, L. L. Shui, and D. M. Deng, Opt. Express **30**, 11331 (2022).

[30] Y. Wu, Z. Lin, C. Xu, D. Xu, H. Huang, J. Zhao, Z. Mo, J. Jiang, H. Yang, L. Zhang, H. Liu, D. Deng, and L. Shui, Phys. Rev. Appl. **17**, 054014 (2022).

[31] Y. Zhang, J. L. Tu, S. L. He, Y. P. Ding, Z. L. Lu, Y. Wu, G. H. Wang, X. B. Yang, and D. M. Deng, Opt. Express **30**, 1829 (2022).

[32] F. Lu, L. Tan, Z. Tan, H. Wu, and Y. Liang, Phys. Rev. A **104**, 023526 (2021).

[33] Y. Liang, L. Tan, N. Liu, K. Chen, H. Liang, H. Wu, B. Luo, F. Lu, H. Chen, B. Zou, and P. Hong, Phys. Rev. Appl. **19**, 014016 (2023).

[34] X. Lu, L. Tan, N. Liu, C. Chen, K. Chen, H. Wu, X. Xia, P. Zhang, P. Hong, B. Zou *et al.*, Phys. Rev. A **108**, 063509 (2023).

[35] L. Tan, N. Liu, F. Lu, D. Liu, B. Yu, Y. Li, H. Wu, K. Chen, Y. Chu, P. Hong, and Y. Liang, Phys. Rev. A **107**, 043501 (2023).

[36] A. Ashkin, J. M. Dziedzic, J. E. Bjorkholm, and S. Chu, Opt. Lett. **11**, 288 (1986).

[37] Z. Liu, X. Wang, and K. Hang, Sci. Rep. **9**, 10187 (2019).

[38] See Supplemental Material at http://link.aps.org/supplemental/10.1103/PhysRevA.109.063515 for the video of trapping particles and moving them around.